#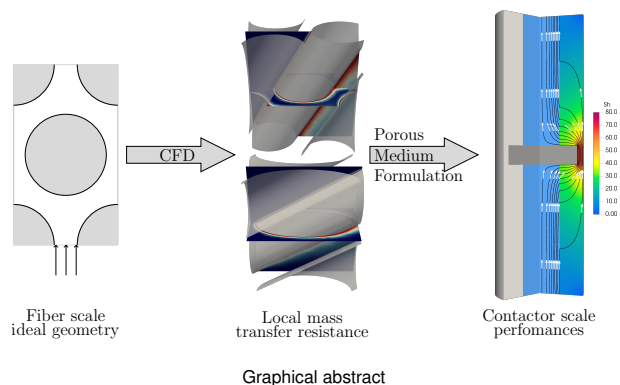 Mass transfer in hollow fiber membrane contactor: Computational fluid dynamics determination of the shell side resistance

Victor Pozzobon[1] ✉ **and Patrick Perré**[1]

[1]LGPM, CentraleSupélec, Université Paris-Saclay, SFR Condorcet FR CNRS 3417, Centre Européen de Biotechnologie et de Bioéconomie (CEBB), 3 rue des Rouges Terres 51110 Pomacle, France

In this work, a fully virtual workflow describing mass transfer at the fiber scale inside of a hollow fiber membrane contactor was used to access overall contactor performances. To do so, fiber geometry was described using limited information. Then a CFD code was used to compute fluid and solute concentration transport over a range of Reynolds number (1 to 400), with no adjustable parameters. Those results compared successfully with a correlation established over numerous experiments in resembling cases. Then, fiber scale CFD results were broadcast to the contactor scale using porous medium formulation. Validation against contactor scale experiments was successful. Finally this workflow was compared to two other numerical approaches, including one relying on case-specific correlation. While all produced satisfactory results, this workflow performed slightly better. Results reported emerge quasi *ex nihilo*, solely considering geometrical properties of the contactor at the fiber scale. Thus, the proposed procedure paves the way toward *in silico* contactor conception, testing and upscalling.

HFMC | Mass transfer | Liquid resistance | CFD | OpenFOAM
Correspondence: *victor.pozzobon@centralesupelec.fr*

Graphical abstract

1. Introduction

Initially developed as artificial lungs, hollow fiber membrane conctactors have now spread to other fields: natural gas sweetening (1), post-combustion carbon capture (2, 3), biogas upgrading (4, 5) or water desalination (6). All of this thanks to their ability to put in non-dispersive contact gas and liquid with a high interfacial area (7–10). Nevertheless, membrane contactors deployment at an industrial scale is conditioned to fine characterisation of the mass transfer phenomena at stake and the relevant upscalling procedures. This is with these objectives in mind that this work was un-

dergone. The context of this study is biogas (CO_2/CH_4) purification, as this technology emerges with great promises in this field (11).

Understanding the phenomena at stake during binary mixture purification can be complex, as pointed out by Fourgerit in (12). All in all, the species fluxes from gas to liquid are functions of three mass transfer resistances: gas phase resistance (within the fiber lumen), membrane phase resistance, and liquid phase resistance. While the first one is classically negligible before the two others, membrane and liquid phase resistances can be of the same order of magnitude. Proper evaluation membrane resistance requires rarefied gas formulation inside the membrane, as shown in (13). Liquid phase resistance is classically determined experimentally (14–17). This evaluation method provides to a global mass transfer resistance value or correlation, readily usable for simple geometry contactor (Fig. 1 (Left)). While valuable, it hinders the possibility to finely account for inner elements, such as baffles (Fig. 1 (Right) and (Middle)) when leading an upscaling procedure. This is all the more detrimental given the fact that those inner elements have consistently been shown to enhance mass transfer inside of the contactor (18).

In addition to the experimental approach, numerical modelling can also contribute to contactor performances determination. In this regard, mass transfer performances can be deduced form fiber scale modelling by coupling local mass tranfer and local flow around a fiber. At this scale, 2D modelling is generally adopted. The codes consider a fiber in its radial direction and describes mass transfer in the different phases. Usually, only one fiber is described. Liquid side can be simplified through mass transfer coefficient or fully resolved with CFD (21–25). Even though precise, those models cannot account for the impact of a bafle, as they only consider the vicinity of a fiber. At the contactor level, 1D and 2D models can be encountered. 1D models split the contactor along its axis and locally estimate mass transfer coefficients in the different phases of the system (gas, membrane, liquid) (26–29). Sadly, these models cannot account for baffle presence as the later induces a 2D flow pattern. 2D models split the contactor in both axial and radial directions (30). Thus they can account for the flow motion around the baffle. Hence they can describe how flow acceleration reduces mass transfer resistance locally. Still both 1D and 2D contactor models need to be provided with mass transfer resistance values or correlation. The later are obtained from experiments, hence
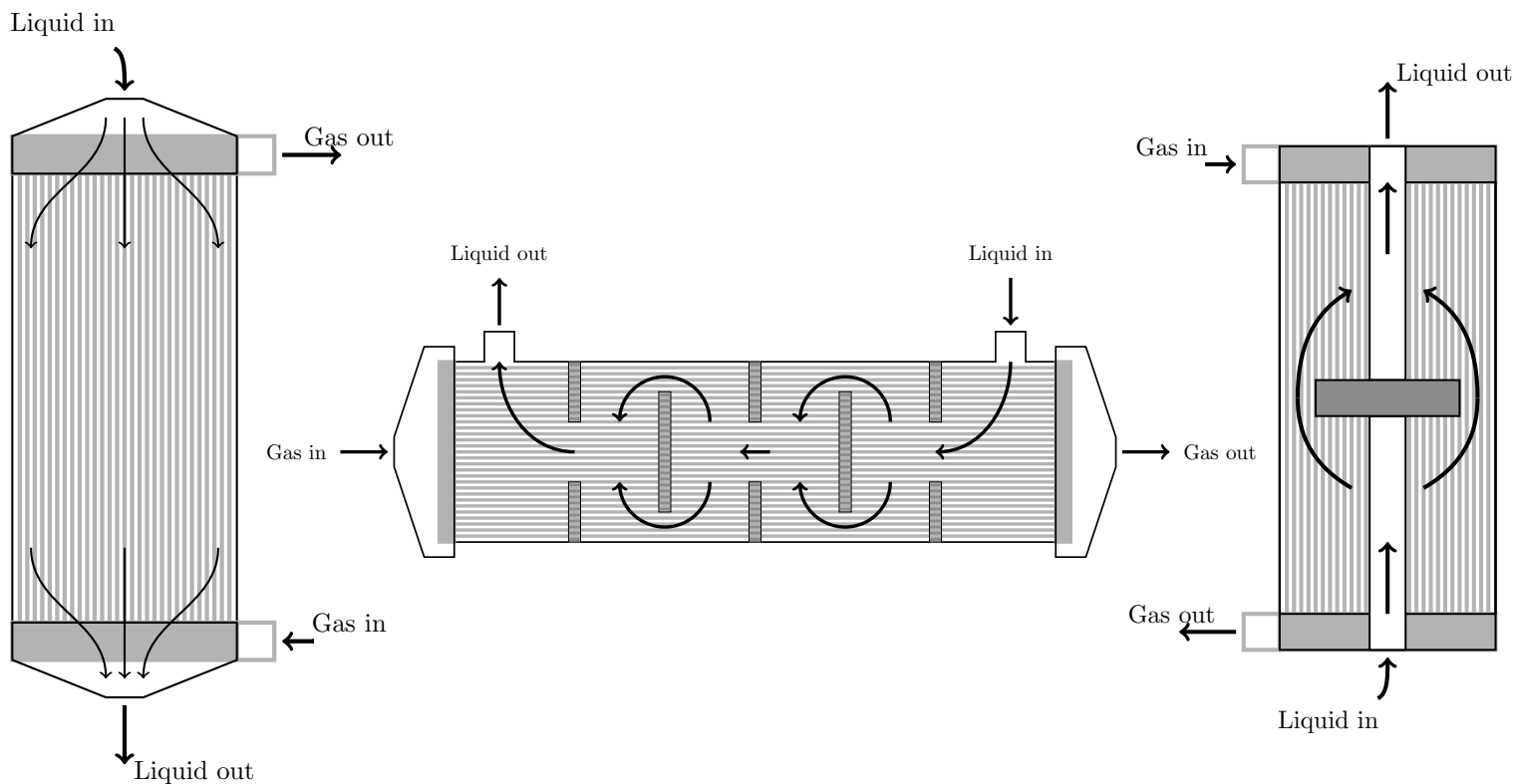
Fig. 1. Different types of hollow fiber membrane contactor. Left - simple countercurrent conctactor (19, 20). Right - single baffle contactor, the one used in this study. Middle - fully baffled contactor (18). Grey lines: fibers, black arrows: flow patterns.

they depend on the operating conditions range over which they were produced.

The purpose of this work was to link local mass transfer resistance around a fiber, obtained numerically, and contactor scale performances. To do so, fiber geometry was described as faithfully as possible, given the limited information available on their packing. Then a CFD code was used to compute fluid flow around the fibers and solute concentration transport - migrating from gas to liquid -. In addition, because the flow is not always parallel of perpendicular to the fibers (Fig. 1 (b) and (c), bent arrows), the effect of the flow to fiber angle on mass transfer resistance was also investigated. During this procedure, no adjustable factor were introduced. The idea of computing macroscopic physical properties based on faithful description of microscopic phenomena is a procedure nowadays rising into power. Indeed it has been made possible over the past decade thanks to the increase in computational power. It was successfully applied to granlunar media, packed or even rocks permeability determination (31–33), heat exchanger (34–36), membrane for distillation (37) or static mixer design (38, 39).

In order to assess the reliability of the proposed workflow, it was validated at two different scales. The first one was the fiber scale. Considering that the fibers packed inside of the contactor form a bundle of tubes, it was possible to compare the CFD results to established correlations. To do so we chose to rely on well established Whitaker's work (40), who reviewed the literature and proposed correlation (Eq. 1, valid for Reynold below 200 and Schmidt between 0.7 and

760, shell side porosity below 0.65) for a flow configuration perpendicular to a bundle of staggered tubes. One should note that this work is reported using Whitaker's terminology, meaning that Reynolds and Sherwood numbers definitions (Eq. 2 and 3) take into account the porosity of the fiber packing (ϵ). In terms of wording, we used the mass transfer coefficient (k) in addition to the mass transfer resistance, the one being the inverse of the second.

$$Sh = 2Re^{1/2}Sc^{1/3} \tag{1}$$

$$Re = \frac{\frac{Q}{S_{in}}d_{fo}}{\nu(1-\epsilon)} \tag{2}$$

$$Sh = \frac{kd_{fo}}{D}\frac{\epsilon}{1-\epsilon} \tag{3}$$

$$Sc = \frac{\nu}{D} \tag{4}$$

The second validation step took place at the contactor scale, using previously published experiments (30). For this, we used pure gas absorption experiments, as this configuration nullifies gas and membrane phase mass transfer resistance, leaving only the liquid one. Full CFD description of a contactor was not an option. Thus, we relied on local porous medium approach already developed in (12, 30). In short, the contactor was considered as a porous medium governed by Darcy's law. Still one should that note that because of fiber alignment (Fig. 1 (b)), the bundle has to be considered as an
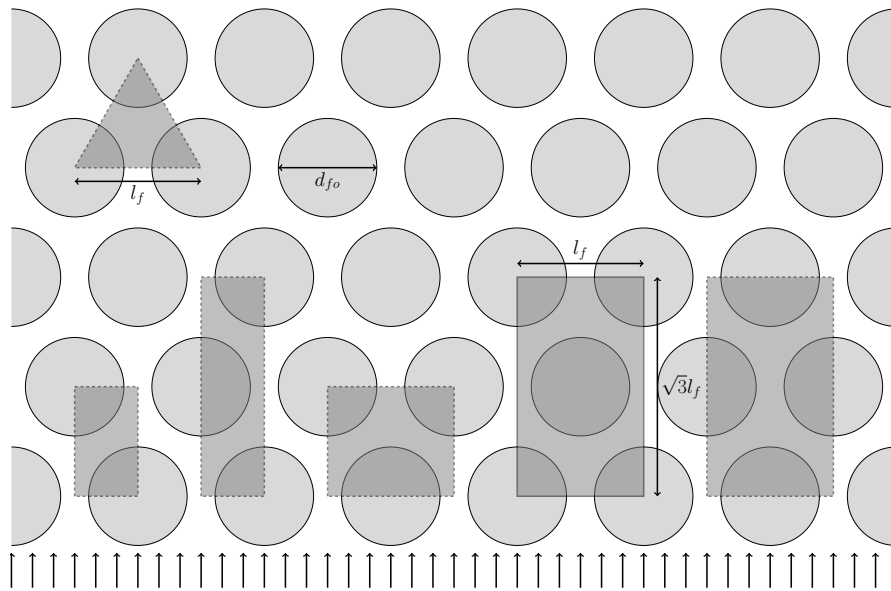
Fig. 2. Fiber hexagonal packing schematic, cut view observed from the top. Shaded areas: sub elements. Dashed edges; possible ones, continuous edge: chosen one. Upward flow

anisotropic porous medium. With this approach, local velocity (hence Reynolds) values and local flow to fiber angle were obtained and correlated to local Sherwood values computed in the first part of this work. Hence, the contactor model did not rely on a correlation but directly on fiber scale CFD results. Finally, these predictions were confronted to experimental observations as well as compared to other numerical procedures.

2. Fiber packing and computational geometry

The hollow fiber membrane contactor used in this study was the Liqui-Cel Extra-Flow 2.5x8" cartridge fitted with type X-50 fibers. Using manufacturer data and other researchers work, it was possible to assess for the inner geometry of the contactor. The parameters used for the coming calculations are summarized in Table 1. On one hand, given the fact that the cartridge holding the fiber has a torus shape, one can compute its cross sectional area (knowing its effective inner and outer diameters). On the other hand, effective fiber cross sectional area can be determined by multiplying individual fiber cross section by the number of fiber. The ratio of those two quantities yielding the fiber packing compactness (Eq. 5):

$$a = \frac{N_f \pi \dfrac{d_{fo}^2}{4}}{\pi \dfrac{d_{co}^2 - d_{ci}^2}{4}} \simeq 0.55 \tag{5}$$

In order to go one step further and determine the actual fiber center to center distance (l_f), one has to assume a packing. In our case, we assumed classical hexagonal packing of cylinders. Even though this assumption can be discussed (43–45), it seemed to be the only reasonable assumption without further knowledge. Figure 2 presents a schematic view of this packing as well as some of its basic elements.

The spacing can easily be determined considering a triangular sub part of the packing. The compactness of this element is a function of l_f and d_{fo}, as given in Eq. 6. In our case, with a compactness of 0.55 (thus a shell side porosity ϵ of 0.45) and an outer fiber diameter of 300 µm, the fiber center to center distance was about 385 µm.

$$a = \frac{\pi \dfrac{d_{fo}^2}{8}}{\dfrac{\sqrt{3}}{4} l_f^2} \tag{6}$$

Now that the inner geometry of the contactor has been determined, the question of the computational domain for the study can be addressed. From a purely mathematical perspective, a lot of possibilities exists - the main constraint being to reproduce the larger domain through symmetry planes. Luckily, this packing features numerous symmetry planes. Figure 2 reports some of the base units that could be used for flow computation. In our case, we favoured the fourth one as base unit for our geometries. The main reason for this choice was that it contains a fiber in full in its core. Thus, the wake behind the fiber can be resolved by the solver.

Before moving on, two comments have to be drawn. First, we only considered a base unit of the geometry. Thus proper computational domain size convergence would have to be led. This, in order to identify how many time this base units has to be duplicated in order to see computed value convergence. Second, the former comment was drawn on Figure 2 basis, i.e. an upward flow perpendicular to the fibers leading to a purely 2D geometry. This configuration is only one of the many possible inside an hollow fiber membrane contactor. Indeed, as presented in Figure 1, flows can take a wide variety of angle with respect to the fibers. In order to cover the extend of the possible flow configurations, our computations were carried out in 3D with varying flow to fiber inclination angle, namely 0, 15, 30, 45, 60 and 90°. All in all,

Characteristic	Symbol	Value	Reference
Fiber outer radius	d_{fo}	300 μm	Membrana datasheet
X-50 fiber membrane porosity	ϵ_f	0.4	Membrana datasheet
X-50 fiber membrane thickness	τ_f	40 μm	Membrana datasheet
X-50 fiber membrane tortuosity	τ_f	3	Membrana datasheet
Cartridge effective outer diameter	d_{co}	$4.64 \ 10^{-2}$ m	(41)
Cartridge effective inner diameter	d_{ci}	$2.10 \ 10^{-2}$ m	(41, 42)
Number of fiber	N_f	10200	(42)
Fiber external specific surface area	s	7334 m^2/m^3	(30)

Table 1. Cartridge and bundle of fiber characteristics for Liqui-Cel Extra-Flow 2.5x8" X-50 fiber type contactor

the base unit dimensions were l_f, $\sqrt{3}l_f$, $\sqrt{3}l_f$ and over x, y and z respectively. The choice of the base unit height being discussed in the coming section.
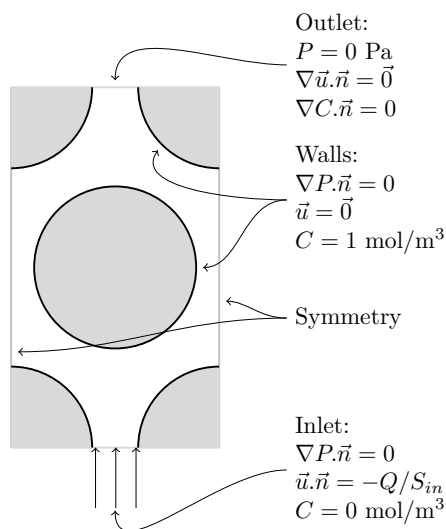

Fig. 3. Schematic view of the case setup for a base unit in the case of 0° inclination angle. Upward flow

3. Flow model

Fluid flows around the fibers were calculated using incompressible steady state Navier-Stokes equations (Eq. 7 and 8), with no body force. The choice of steady state simulation was based on characteristic times comparison. Three times were considered:

- the time for liquid and gas to invade the contactor when starting up (volume divided by flow rate) is about 2.5 seconds for the lowest flow rate used in this study

- the time for gas to diffuse through a liquid filled membrane ($e_f^2/\dfrac{D\epsilon_f}{\tau_f}$, with D taken as CO_2-liquid water diffusion coefficient, D = $1.71 \ 10^{-9}$ m^2/s (46)) is around 7.0 seconds

- time for which contactors are operated is usually higher than one hour

Operation time being much higher than the times required for the physical phenomena to set up, transient state was dis-

carded in our study. As aforementioned, because the fibers are closely packed, turbulence is unlikely to happen in actual operating conditions. Thus, the flow was assumed to be laminar over the whole range of inlet flow rates. This assumption alleviated the question of which turbulence model to chose. Yet it would have to be later validated.

$$\nabla . \vec{u} = 0 \qquad (7)$$

$$\vec{u}\nabla . \vec{u} = -\frac{\nabla P}{\rho} + \nu \nabla^2 \vec{u} \qquad (8)$$

Dissolved mass transport was computed using classical steady state transport equation (Eq. 9). This concentration was assumed to be low enough not to have any retroaction on the flow (viscosity variation, buoyancy effects nor normal velocity at the interface):

$$\nabla . (\vec{u}C) = -\nabla . (-D\nabla C) \qquad (9)$$

At the inlet, the flow rate and a null solute concentration were specified while the pressure was set freely by the solver:

$$\vec{u}.\vec{n} = -\frac{Q}{S_{in}} \qquad (10)$$

$$\nabla P.\vec{n} = 0 \qquad (11)$$

$$C = 0 \text{ mol/m}^3 \qquad (12)$$

At the outlet, the fluid and the solute could leave the domain freely under constant null relative pressure condition:

$$\nabla \vec{u}.\vec{n} = \vec{0} \qquad (13)$$

$$P = 0 \text{ Pa} \qquad (14)$$

$$\nabla C.\vec{n} = 0 \qquad (15)$$

On the walls, no slip condition was applied to the fluid motion, while the concentration was set to a constant value of unity:

$$\vec{u} = \vec{0} \qquad (16)$$

$$\nabla P.\vec{n} = 0 \qquad (17)$$

$$C = 1 \text{ mol/m}^3 \qquad (18)$$

Figure 3 presents an upward view of the computational domain and the associated boundary conditions in the case of 0° inclination angle.

Symmetry boundary conditions were used on lateral sides, bottom and top of the computational domain. While perfectly valid for the sides, this has to be discussed for the bottom and the top of the domain in the case of angled geometries. Indeed, this condition assumed that the domain was a subset of an infinite periodic domain, which was not the case vertically for tilted configurations. Other authors have already discussed the question of the choice of the lateral boundary conditions in this kind of case (47). They showed that this choice has a minor impact provided the mesh it sufficiently refined - which was thought to be the case here. Following their recommendations, we used symmetry boundary conditions for the bottom and top boundaries. Nevertheless, the impact of this choice would be later assessed by considering the results obtained on computational domains of increasing vertical size. Still a base unit height had to be proposed first. In our case, we chose to use the same value as the base unit length.

In addition to boundary conditions, physical properties had to be specified. They were taken has those of water at 20 °C for the fluid ($\nu = 1.00 \ 10^{-6}$ m^2/s) and CO_2 for the solute ($D = 1.71 \ 10^{-9}$ m^2/s, yielding a Schmidt number of 649, within Whitaker's correlation validity range). Finally, the mass transfer coefficient was accessed through the classical equation for convective mass transfer (Eq. 19). k value could be computed using the integral of the solute flux leaving the domain (Ψ_{out}), the fiber surface (S_f) and a reference solute concentration difference ($C_w - C_{ref}$, with $C_w = 1$ mol/m^3 and $C_{ref} = 0$ mol/m^3). From this, Sherwood number could also be computed (Eq. 3).

$$\int_{S_{out}} \Psi_{out} dS = k S_f (C_w - C_{ref}) \qquad \textbf{(19)}$$

4. Numerical procedures

4 1. Meshing and computing

The computations were led using the open source CFD framework OpenFOAM (48) (18.12+ release). This framework offers solutions to both mesh the geometry and later compute the flow. In our case, we used the automatic meshing program called *snappyHexMesh* to mesh the fluid domain in-between the fibers. This meshing algorithm works in three key stages which have been extensively described and illustrated in (49). Only the core of those stages are summarize hereinafter:

- first, a background hexahedral mesh is generated. Fibers are superimposed over this background mesh. The algorithm detects the cells that are intersected by the fibers surface and then divides them in the middle into 8 smaller cells. This creates a mesh refinement close to the fiber surface. This step is repeated a number of time prescribed by the operator. Once this step is completed, cells that have less than 50 % of their volume inside of the fluid domain are deleted.

- then, the points of the mesh close the fibers surface are moved so that they snap onto it. This step ensures that the boundary surfaces of the mesh are as close as possible to the prescribed geometry.

- finally, layers of cells are added near the walls to better capture hydrodynamics and mass transfer boundary layers
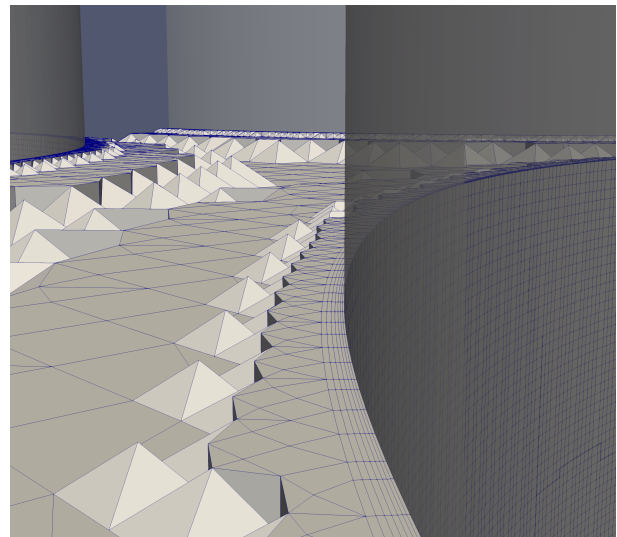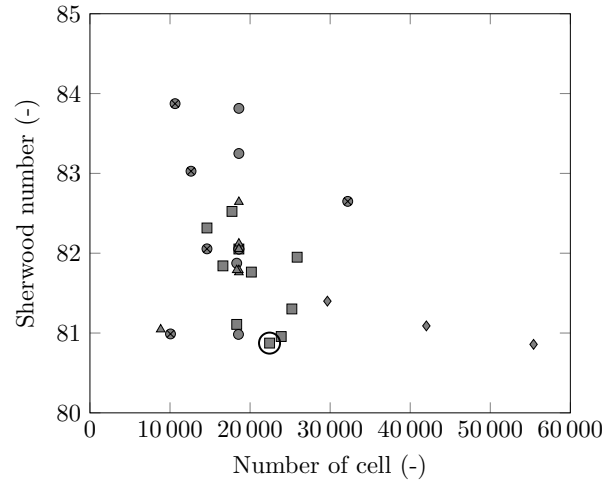

Fig. 4. Top - mesh convergence, for 0° inclination Reynolds 100 setup. Marks: diamonds - increasing base mesh resolution, crossed circles - increasing refinement level, squares - increasing number of boundary layers, triangles - increasing total boundary layer thickness, open circles - increasing boundary layers expansion ratio. Circle point: chosen one. Bottom - cut view of the 3D mesh for 0° flow to angle inclination. View point: in-between the fibers

In our case, the key parameters of this procedure were: the number of consecutive divisions prescribed by the operator, the initial mesh size and the number and shape of cells boundary layer. They are discussed in the coming Section.

Once the mesh had been generated, the fluid flow equations were computed with *simpleFoam* solver, which uses SIMPLEC algorithm to compute a Navier-Stokes equations steady state solution. After fluid flow calculation, solute concentration was computed using *scalarTransportFoam* solver. Second order schemes, with flux limiter, were used for spatial discretization. Convergence criteria for all solutions were set

at 10^{-6}. Meshing and computations steps were both CPU and RAM intensive. To face the need for computational power, we used part the ROMEO cluster - 8 nodes, 16 cores (Intel Skylake 6132 @ 2,6 GHz) and 32 Go DDR4 per node -. The classical run time was 6 hours, the three quarter of it being the mesh generation procedure.

4 2. Mesh and computational domain size convergences

Mesh convergence was led on one base unit, at $0°$ inclination angle for a Reynolds number of 100. This value was chosen as we know from former study (30) that the maximum Reynolds number value encountered in our experimental setup was 54. By validating at high Reynolds value we ensured that the mesh was suited for lower values. Indeed, higher Reynolds values correlate with thinner boundary layers, hence stricter validation criterion. The monitored output was the Sherwood predicted number.

The parameters impacts were explored by varying around a reference setup: base mesh cell size 10 μm (1/30 of the fiber diameter), 3 levels of refinement following surface detection, addition of 3 boundary layers, with relative size of 15 % and expansion factor of 1.2. All the parameters were varied. In order to speed this process up, it was led on a 2D prototype geometry, as the $0°$ inclination case was purely 2D. This allowed to dramatically reduce the mesh size to about 20 000 cells while being 8 millions cells on the 3D production runs. It addition, this protocol saved a considerable amount computation time. Indeed it cut the runtime by a factor 60, mainly by reducing the mesh generation CPU cost.

The results of this exploration are reported in Figure 4 (Top). Even though intricated, the impact of meshing procedure on Sherwood number can be extracted from this figure. On the on hand, parameters increasing the cell density far from the wall (base mesh resolution - diamonds - and refinement level - crossed circles -) had only little impact on the computation of the Sherwood number, even though they considerably increased the number of cell. On the other hand, parameters increasing the cell density in the vicinity of the wall (the others) had a notable influence on the computation. This can easily be explained by the fact that the key criterion was refinement close to the wall, where the mass solute concentration gradient had to be precisely evaluated. As a general rule, too coarse meshing next to the wall induced improper solute gradient evaluation hence Sherwood number overestimation. In our case, among the sets of parameters yielding values close to the one expected using Whitaker's work (Sh = 80.4 at Re = 100), we chose the circled one (Sh = 80.9, for base mesh cell size 10 μm, 3 levels of refinement, addition of 7 boundary layers, with relative size of 15 % and expansion ratio of 1.2). A visualization of this mesh is available in Figure 4 (Bottom). As one can see, high aspect ratio between near wall cells and bulk flow cells is obtained with this meshing procedure.

Once a proper meshing procedure had been established, the question of computational domain size could be addressed. The computational domain was extended in two di-

rections: the direction of the flow, to assess for the influence of the inlet conditions (plug flow) and the direction perpendicular to the flow, to assess for the top and bottom symmetry boundary condition influence. We used the $30°$ inclination, Reynolds 100 3D setup for these tests. For both direction, base units were reproduced up to 5 times. In the direction of the flow, extracted amount of solute showed a perfectly linear increase (5 points, R-squared of 0.99997). This shows that a single base unit in this direction was already enough. In the direction perpendicular flow, extracted amount of solute also showed a perfectly linear increase (5 points, R-squared of 0.9997). This showed that the chosen height (l_f, same as the base unit length) was already high enough to nullify the impact of the symmetry boundary condition used on the bottom and top of the computational domain.

Even though it could have been interesting to reduce the size of the base unit, this would have been done purely out of numerical interest, which lied outside of the scope of this work.

Finally, confident in our mesh, we used the code to assess for influence of increasing Reynolds number value over Sherwood number value. The explored range lied between Reynolds number value of 1 to 400, as values encountered in contactor ranged form 3 to 54. The investigation above Reynolds 100 aimed at determining the robustness of the laminar flow assumption.

5. Fiber scale results

Computation was led for Reynolds numbers ranging from 1 to 400 on 7 different geometries. Figure 5 presents a visualization of solute concentration fields for all the all geometries for a Reynolds number of 1. As one can see, the code qualitatively reproduced the phenomena that were expected, namely, a sharp gradient in the part of the fiber facing the flow, and a looser one in its wake. In addition, from the horizontal cut planes, one can have a closer look at the wake structure. A slightly longer wake could be observed for the central cylinder. This can be explained by the fact that for this cylinder, the boundary layer can develop from the stagnation point until the back of the cylinder, while only on half of it for the two first cut cylinders. Still, it was though to have only a minor effect on the Sherwood number determination, as domain extension in the flow direction (Sec. 4.2) yielded an highly linear increase (R-squared of 0.99997). From this, one can also see the impact of the closeness of the packing. Classically, a single cylinder wake would exhibit smooth solute concentration decrease. This is not the case here, as surrounding fibers forced the fluid to accelerate on the back on the central fiber, constraining the boundary layer. This also explains why lengthening the computational domain in Section 4.2 led to a perfectly linear increase of the solute flow. Indeed, bulk solute concentration remained almost null in all the consecutive base units ensuring gradient, hence transfer potential, conservation.

Confident in the fact that the solver produced no artefacts, a more quantitative comparison was undergone. To do so, computed Sherwood number values were plotted versus Reynolds
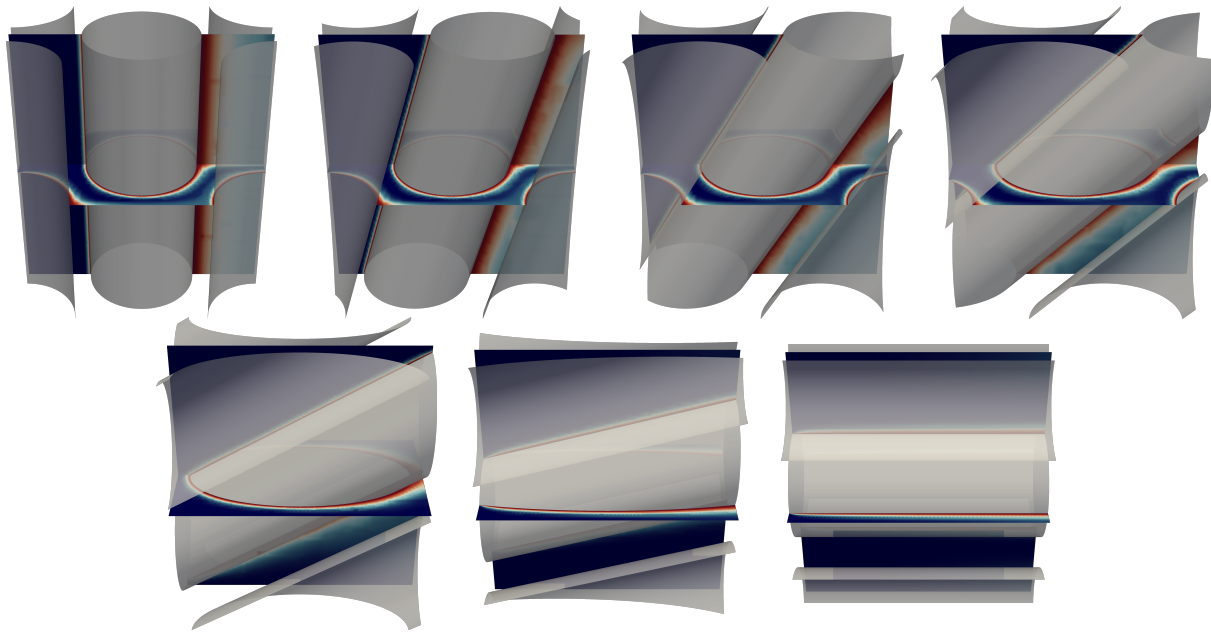
Fig. 5. Visualization of the solute concentration for all the inclination angles (starting by 0°) for a Reynolds number of 1. Flow direction: left to right. Colormap: solute concentration, red: 1 mol/m^3, deep blue: 0 mol/m^3
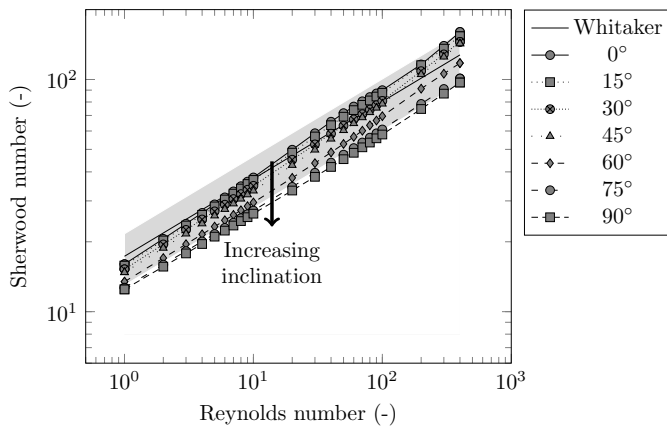

Fig. 6. Sherwood number versus Reynolds number for all the geometries and Whitaker correlation (shaded area $\pm$ 25 %) - to compare to 0° inclination -

number and compared to Whitaker correlation (Fig. 6). As Whitaker underlined log-log plots tend to minimize the perception of the experimental data spread (around $\pm$ 25 %). Thus our results are plotted with a shaded area of this magnitude. Furthermore, one should note that, strictly speaking, only 0° inclination could be compared to Whitaker's correlation, as other geometries were different from those he used.

First of all, a good agreement was observed over the whole range of Reynolds numbers. The 0° inclination results were encompassed in the suggested $\pm$ 25 % range and the trend was well reproduced. Still a minor deviation could be noted on the slope. This was especially true for Reynolds number values above 200. Those high Reynolds number values have to be interpreted with caution, as the mesh may not have been perfectly suited for those cases. Still the predicted Sherwood values shifted upward, which was in agreement with Whitaker's work. Indeed, he proposed two correlations: one for low Reynolds numbers (the one we compare to) and

one for high Reynolds numbers (with a steeper slope than the first). The transition between the two being located for Reynolds number of the order of magnitude of 100. Physically this transition corresponds to the point where vortices start to appear behind the cylinders.

Second, inclining the fibers reduced the Sherwood number values. This could be explained by the fact that increasing the inclination changed the progressively the setup from a cylinder facing a flow to a cylinder along the flow. In terms of boundary layer thickness, i.e. solute concentration gradient, the later configuration favoured larger boundary layers (as in can be seen on Fig. 5), hence looser gradients and lower mass transfer.

Furhermore, even though the mesh may not have been suited for this exploration, results were produced for Reynolds number higher than 100. The objective was to determine the robustness of the laminar flow assumption. The laminar to turbulent transition range of Reynlods number for this kind of geometries lies between 400 and 1000 (50)). The solver showed signs of instability (longer run time, hard to reach convergence) from Reynolds number value above 700. The lack of turbulence model may be a valid explanation for this behaviour. Still, as the maximum local Reynolds value encountered in a contactor is around 54, the laminar flow assumption stood.

Finally, the Sherwood number values produced by this procedure were then stored in a two-entry databank. The first entry was Reynolds number value, the second, the flow to fiber angle.

6. Contactor scale upscaling

6 1. Upscaling procedure

Once confident in the fiber scale results, the upscaling of this approach to the whole contactor was undergone. As
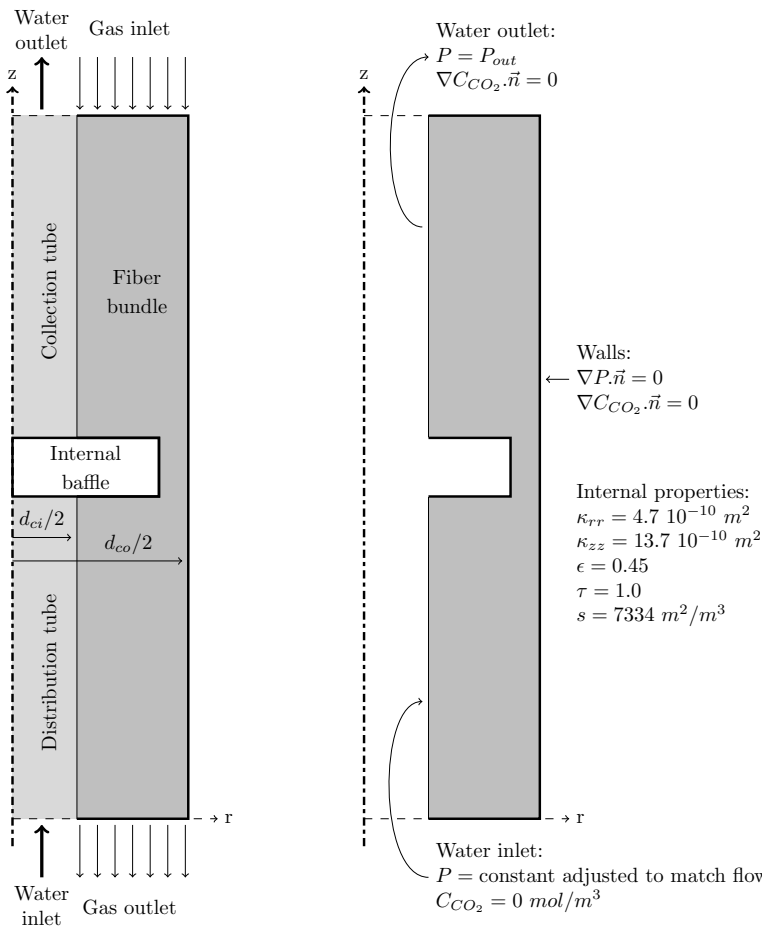
Fig. 7. Schematic view of the contactor and associated numerical setup

Fig. 8. Visualisation of the porous medium code integrating fiber scale CFD results (3D broadcasting for illustration purposes only). Operating conditions: liquid flow rate - 120 l/h, liquid pressure - 5.5 bar, gas flow rate - 1 Nm^3/h, gas pressure - 5 bar. Colormap: Sherwood number. Continuous lines: liquid flow streamlines

aforementioned, full CFD study on the contactor was out of reach, as a partial section of a fiber already required 8 millions cells to be properly described. Luckily, Fougerit proposed a low computational cost method accounting locally for mass transfer inside of a contactor (12, 30). Only its core stages of this procedure are recalled here. The contactor was considered as a 2D anisotropic (because of fiber orientation) porous medium governed by Darcy's law (Eq. 20). The liquid flow inside of the contactor was assumed to be incompressible (Eq. 21) with constant physical properties. Solute concentration was tracked inside the contactor using classical porous media formulation (Eq. 22), where the last term of the equation accounted for gas to liquid solute transfer. A schematic of the geometry, the associated numerical setup and porous medium physical properties are available on Figure 7. Thanks to this formulation it was possible to resolve velocity field locally, hence to access local values of the Reylnolds number. This is crucial as the contactor featured a central baffle, considerably accelerating the flow locally. In addition, knowing that the fibers were stacked vertically (Fig. 1 (b)), the flow to fiber angle could be computed, locally again. These two parameters were used to determine the associated Sherwood number value, thanks to the databank compiling fiber CFD results. Even though numerous (168) runs were produced, both Reynolds and flow to fiber angle values in the databank did not match the exact values
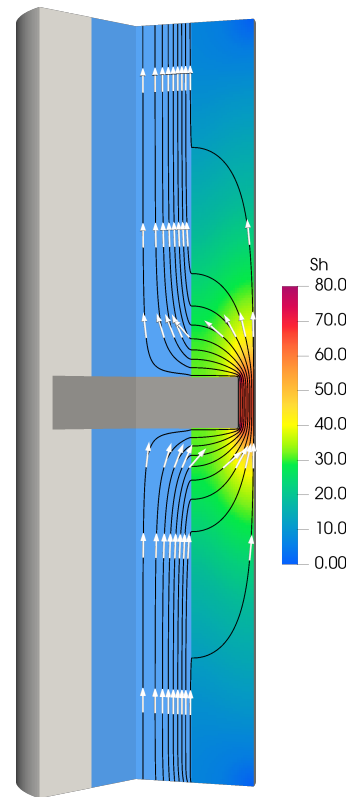
encountered within the contactor. Thus, for each cell, local Sherwood number was computed using a bilinear interpolation between the closest values of Reynolds number and flow to fiber angle.

$$\vec{u} = -\frac{\bar{\bar{\kappa}}}{\mu}\nabla P \tag{20}$$

$$\nabla.\vec{u} = 0 \implies \nabla.-\frac{\bar{\bar{\kappa}}}{\mu}\nabla P \implies \nabla.\nabla P = 0 \tag{21}$$

$$\nabla.(\vec{u}C_{CO_2}) = -\nabla.(-\frac{\epsilon D_{CO_2}}{\tau}\nabla C_{CO_2})$$
$$+ \frac{Sh D_{CO_2}}{d_{fo}}\epsilon s(C_{CO_2,ref} - C_{CO_2}) \tag{22}$$

This set of equation was solved using an homemade OpenFOAM solver. First, pressure equation was solved, then velocity was computed using Darcy's law. Finally, solute transport equation was solved. Space discretization was ensured using second order schemes. This procedure was repeated iteratively until all residues fell below 10^{-6}.

6 2. Experimental reference

In order to validate his model, Fougerit produced a set of 11 runs during which pure CO_2 was absorbed into water.
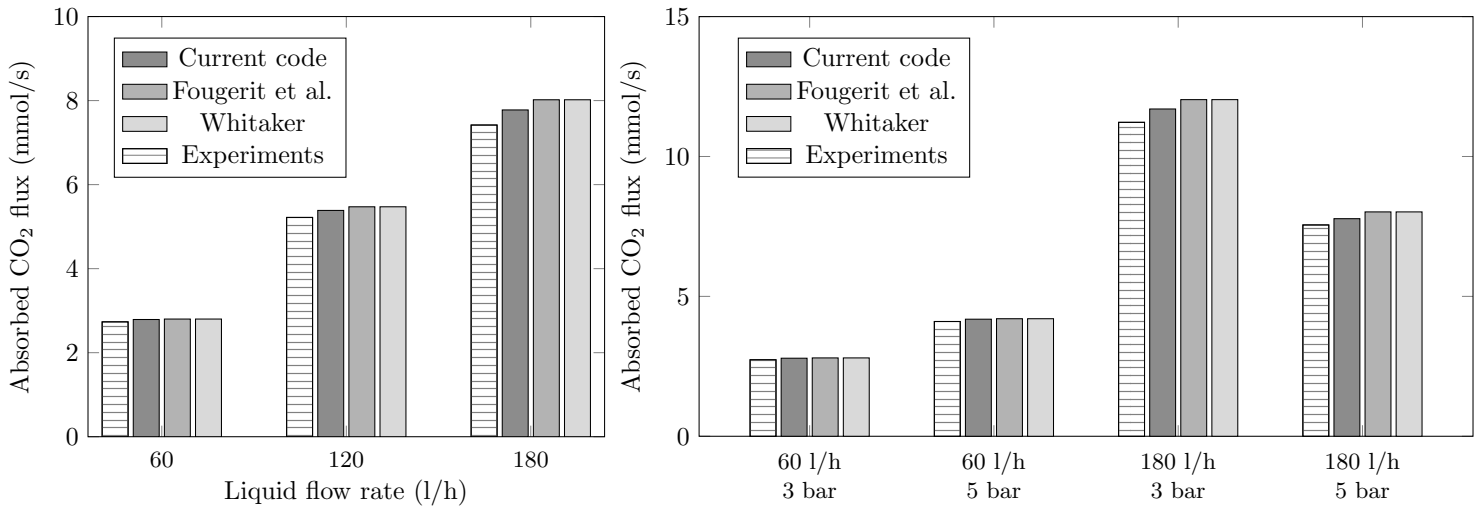
Fig. 9. Numerical predictions and experimental observations over Fougerit's dataset. Left - liquid pressure - 5.5 bar, liquid flow rate - varying, gas pressure - 3 bar, gas flow rate - 700 Nl/h. Right - liquid pressure - 5.5 bar, liquid flow rate - varying, gas pressure - varying, gas flow rate - 700 Nl/h

Model	SSE (10^{-6} (mol/m^3)^2)	$\frac{SSE}{SSE_{Current\ work}}$
Current work	0.9019	1
Fougerit's correlation	1.167	1.294
Whitaker's correlation	2.193	2.432

Table 2. Sum of Squared Errors for the three different numerical approaches over the 11 points of Fougerit's dataset

The advantage of working with pure gas was that the sole resistance to mass transfer was located in the liquid phase. Over his experiments, both gas and liquid flow rates as well as liquid pressure were varied. CO_2 pressure was also manipulated in order to control $C_{CO_2,ref}$ term in Eq. 22, as $C_{CO_2,ref} = \frac{P}{RT}$. Finally, using this batch of experiments, Fougerit optimized a correlation linking local Sherwood, Reynolds ($Re_{\vec{u}}$ being the Reynolds number based on local velocity value) and Schmidt numbers (Eq. 23, modified to be consistent with Whitaker terminology):

$$Sh = 3.45 \frac{\epsilon}{1-\epsilon}(Re_{\vec{u}}(1-\epsilon))^{0.42}Sc^{1/3} \quad \textbf{(23)}$$

6 3. Contactor scale results

The porous medium model presented in Section 6.1 was used to reproduce the 11 experimental runs. Figure 8 presents a visualisation of the flow and the associated Sherwood number field at the contactor scale. As one can see, the Sherwood number was, as expected, at its maximum around the baffle. Once confident in the flow description, a more quantitative validation was undergone. To do so, our workflow results were compared to, in turn, experiments, results produced by Fougerit's correlation and results produced by Whitaker's correlation. All those results are plotted in Figure 9. All the numerical approaches successfully captured both experimental trend and absolute values. From this figure, it becomes obvious that sole graphical comparison was not enough. Then, another metric had to be used to compare the three numerical approaches. To do so, we chose to rely on the Sum of Squared Errors (Eq. 24).

$$SSE = \sum_{i=0}^{n}(\Psi_{exp} - \Psi_{num})^2 \quad \textbf{(24)}$$

SSE computations are available in Table 2. As one can see, our workflow and Fougerit's correlation yielded the best results, Whitaker's correlation being behind (producing nonetheless very good results). Our workflow represents a slight improvement over Fourgerit's work (about 29 % on SSE). This can be seem as surprising given the fact that Fougerit used an optimizer to produce his correlation, thus found the best fitting parameters. Still, the explanation comes from the fact that our approach is able to take into account flow to fiber angle, while his cannot. While comparing those results, one last though should be be kept in mind. Fougerit's and Whitaker's correlations relied on experiments to reproduce experiments. Our workflow made those results emerge quasi *ex nihilo*, solely considering geometrical properties of the contactor at the fiber scale.

7. Conclusion

In this work, a fully virtual workflow describing mass transfer at the fiber scale inside of a hollow fiber membrane contactor was to access overall contactor performances. To do so, fiber geometry was described as faithfully as possible given the limited information available on their packing. In addition flow to fiber inclination was taken into account through different geometries. Within these geometries CFD code was used to compute fluid and solute concentration transport over a range of Reynolds number (1 to 400). All this done solely using known physical properties. At this point, a first com-

parison with a correlation established over numerous experiments in similar cases was successfully undergone.

In a second step, fiber scale CFD results were provided to another code describing the whole contactor. Using this approach, it was possible to broadcast CFD results to the contactor scale. Here again, validation against experimental results was successful. Our workflow even represents a slight improvement over former work led using correlation produced by a numerical optimizer.

As concluding though, one should bare in mind that our workflow made those results emerge quasi *ex nihilo*, solely considering geometrical properties of the contactor at the fiber scale. Thus, it paves the way toward *in silico* contactor conception, testing and upscalling.

Acknowledgements

References

1. Mohamed H. Al-Marzouqi, Sayed A. M. Marzouk, and Nadia Abdullatif. High pressure removal of acid gases using hollow fiber membrane contactors: Further characterization and long-term operational stability. *Journal of Natural Gas Science and Engineering*, 37:192–198, January 2017. ISSN 1875-5100. .

2. Shuaifei Zhao, Paul H. M. Feron, Liyuan Deng, Eric Favre, Elodie Chabanon, Shuiping Yan, Jingwei Hou, Vicki Chen, and Hong Qi. Status and progress of membrane contactors in post-combustion carbon capture: A state-of-the-art review of new developments. *Journal of Membrane Science*, 511:180–206, August 2016. ISSN 0376-7388. .

3. Paul Feron, editor. *Absorption-Based Post-Combustion Capture of Carbon Dioxide.* Woodhead Publishing, Duxford, UK, 1 edition edition, July 2016. ISBN 978-0-08-100514-9.

4. Steffen Vogler, Axel Braasch, Gerhard Buse, Sören Hempel, Jürgen Schneider, and Martin Ulbricht. Biogas Conditioning Using Hollow Fiber Membrane Contactors. *Chemie Ingenieur Technik*, 85(8):1254–1258, 2013. ISSN 1522-2640. .

5. Andrew McLeod, Bruce Jefferson, and Ewan J. McAdam. Quantifying the loss of methane through secondary gas mass transport (or 'slip') from a micro-porous membrane contactor applied to biogas upgrading. *Water Research*, 47(11):3688–3695, July 2013. ISSN 0043-1354. .

6. Andy Chenggui Sun, Walter Kosar, Yufeng Zhang, and Xianshe Feng. Vacuum membrane distillation for desalination of water using hollow fiber membranes. *Journal of Membrane Science*, 455:131–142, April 2014. ISSN 0376-7388. .

7. Michel Roustan. Transferts gaz-liquide dans les procédés de traitement des eaux et des effluents gazeux. 2003.

8. Jessy Elhajj, Mahmoud Al-Hindi, and Fouad Azizi. A Review of the Absorption and Desorption Processes of Carbon Dioxide in Water Systems. *Industrial & Engineering Chemistry Research*, 53(1):2–22, January 2014. ISSN 0888-5885. .

9. VICTOR A Atiemo-Obeng, WR Penney, and Piero Armenante. Solid-liquid mixing. *Handbook of industrial mixing: Science and practice*, pages 543–584, 2004.

10. Jing-Liang Li and Bing-Hung Chen. Review of CO2 absorption using chemical solvents in hollow fiber membrane contactors. *Separation and Purification Technology*, 41(2):109–122, February 2005. ISSN 1383-5866. .

11. Bouchra Belaissaoui and Eric Favre. Novel dense skin hollow fiber membrane contactor based process for CO2 removal from raw biogas using water as absorbent. *Separation and Purification Technology*, 193:112–126, March 2018. ISSN 1383-5866. .

12. Valentin Fougerit, Victor Pozzobon, Dominique Pareau, Marc-André Théoleyre, and Moncef Stambouli. Experimental and numerical investigation binary mixture mass transfer in a gas – Liquid membrane contactor. *Journal of Membrane Science*, 572:1–11, February 2019. ISSN 0376-7388. .

13. W. Kast and C. R. Hohenthanner. Mass transfer within the gas-phase of porous media. *International Journal of Heat and Mass Transfer*, 43(5):807–823, March 2000. ISSN 0017-9310. .

14. François-Xavire Pierre, Isabelle Souchon, Violaine Athes-Dutour, and Michèle Marin. Membrane-based solvent extraction of sulfur aroma compounds: influence of operating conditions on mass transfer coefficients in a hollow fiber contactor. *Desalination*, 148(1):199–204, September 2002. ISSN 0011-9164. .

15. P. Schöner, P. Plucinski, W. Nitsch, and U. Daiminger. Mass transfer in the shell side of cross flow hollow fiber modules. *Chemical Engineering Science*, 53(13):2319–2326, July 1998. ISSN 0009-2509. .

16. Ju-Meng Zheng, Zheng-Wei Dai, Fook-Sin Wong, and Zhi-Kang Xu. Shell side mass transfer in a transverse flow hollow fiber membrane contactor. *Journal of Membrane Science*, 261(1):114–120, September 2005. ISSN 0376-7388. .

Latin symbols

a	compactness	-
C	concentration	mol/m^3
D	mass diffusion coefficient	m^2/s
d	diameter	m
e	thickness	m
k	mass transfer coefficient	m/s
l_f	fiber center to center distance	m
N_f	number of fiber	-
$\vec{n}$	normal vector	-
P	relative pressure	Pa
Q	volumetric flow rate	m^3/s
R	Boyle Mariotte constant	J/mol/k
Re	Reynolds number	-
S	surface	m^2
s	specific surface area	m^2/m^3
Sc	Schmidt number	-
T	temperature	K
Sh	Sherwood number	-
$\vec{u}$	velocity	m/s

Greek symbols

ϵ	porosity	-
ν	kinematic viscosity	m^2/s
μ	dynamic viscosity	Pa.s
Ψ	solute flow	mol/s
τ	tortuosity	-
κ	permability	m^2
ρ	density	kg/m^3

Subscripts

CO_2	carbon dioxide
c	cartridge
exp	experimental
f	fiber
i	inner
in	inlet
num	numerical
o	out
out	outlet
ref	reference
rr	radial
w	wall
zz	longitudinal

Other symbols

∇	nabla operator
$\bar{\bar{a}}$	tensor
.	dot product

Table 3. Nomenclature

17. M. Mavroudi, S. P. Kaldis, and G. P. Sakellaropoulos. A study of mass transfer resistance in membrane gas–liquid contacting processes. *Journal of Membrane Science*, 272(1):103–115, March 2006. ISSN 0376-7388. .

18. Karen L. Wang and E. L. Cussler. Baffled membrane modules made with hollow fiber fabric. *Journal of Membrane Science*, 85(3):265–278, December 1993. ISSN 0376-7388. .

19. Hong Joo Lee, Yu Gang Park, Min Kwang Kim, Seung Hwan Lee, and Jung Hoon Park. Study on CO2 absorption performance of lab-scale ceramic hollow fiber membrane contactor by gas/liquid flow direction and module design. *Separation and Purification Technology*, 220:189–196, August 2019. ISSN 1383-5866. .

20. Humberto Estay, Elizabeth Troncoso, René Ruby-Figueroa, and Julio Romero. Assessment of Industrial Modules to Design a GFMA Process for Cyanide Recovery Based on a Phenomenological Model. *Processes*, 6(4):34, April 2018. .

21. Hong-Yan Zhang, Rong Wang, David Tee Liang, and Joo Hwa Tay. Modeling and experimental study of CO2 absorption in a hollow fiber membrane contactor. *Journal of Membrane Science*, 279(1):301–310, August 2006. ISSN 0376-7388. .

22. Yunfei Yan, Zhien Zhang, Li Zhang, Yanrong Chen, and Qiang Tang. Dynamic Modeling of Biogas Upgrading in Hollow Fiber Membrane Contactors. *Energy & Fuels*, 28(9):5745–5755, September 2014. ISSN 0887-0624. .

23. F. Porcheron and S. Drozdz. Hollow fiber membrane contactor transient experiments for the characterization of gas/liquid thermodynamics and mass transfer properties. *Chemical Engineering Science*, 64(2):265–275, January 2009. ISSN 0009-2509. .

24. Nikhil Goyal, Shishir Suman, and S. K. Gupta. Mathematical modeling of CO2 separation from gaseous-mixture using a Hollow-Fiber Membrane Module: Physical mechanism and influence of partial-wetting. *Journal of Membrane Science*, 474:64–82, January 2015. ISSN 0376-7388. .

25. Mohamed H. Al-Marzouqi, Muftah H. El-Naas, Sayed A. M. Marzouk, Mohamed A. Al-Zarooni, Nadia Abdullatif, and Rami Faiz. Modeling of CO2 absorption in membrane contactors. *Separation and Purification Technology*, 59(3):286–293, March 2008. ISSN 1383-5866. .

26. Somnuk Boributh, Suttichai Assabumrungrat, Navadol Laosiripojana, and Ratana Jiraratananon. A modeling study on the effects of membrane characteristics and operating parameters on physical absorption of CO2 by hollow fiber membrane contactor. *Journal of Membrane Science*, 380(1):21–33, September 2011. ISSN 0376-7388. .

27. Wichitpan Rongwong, Cao Fan, Zhiwu Liang, Zhang Rui, Raphael O. Idem, and Paitoon Tontiwachwuthikul. Investigation of the effects of operating parameters on the local mass transfer coefficient and membrane wetting in a membrane gas absorption process. *Journal of Membrane Science*, 490:236–246, September 2015. ISSN 0376-7388. .

28. Sakarin Khaisri, David deMontigny, Paitoon Tontiwachwuthikul, and Ratana Jiraratananon. A mathematical model for gas absorption membrane contactors that studies the effect of partially wetted membranes. *Journal of Membrane Science*, 347(1):228–239, February 2010. ISSN 0376-7388. .

29. Jian-Gang Lu, You-Fei Zheng, and Min-Dong Cheng. Wetting mechanism in mass transfer process of hydrophobic membrane gas absorption. *Journal of Membrane Science*, 308(1):180–190, February 2008. ISSN 0376-7388. .

30. Valentin Fougerit, Victor Pozzobon, Dominique Pareau, Marc-André Théoleyre, and Moncef Stambouli. Gas-liquid absorption in industrial cross-flow membrane contactors: Experimental and numerical investigation of the influence of transmembrane pressure on partial wetting. *Chemical Engineering Science*, 170:561–573, October 2017. ISSN 0009-2509. .

31. Paola Ranut, Enrico Nobile, and Lucia Mancini. High resolution X-ray microtomography-based CFD simulation for the characterization of flow permeability and effective thermal conductivity of aluminum metal foams. *Experimental Thermal and Fluid Science*, 67:30–36, October 2015. ISSN 0894-1777. .

32. S. Jaganathan, H. Vahedi Tafreshi, and B. Pourdeyhimi. A realistic approach for modeling permeability of fibrous media: 3-D imaging coupled with CFD simulation. *Chemical Engineering Science*, 63(1):244–252, January 2008. ISSN 0009-2509. .

33. Romain Guibert, Pierre Horgue, Gérald Debenest, and Michel Quintard. A Comparison of Various Methods for the Numerical Evaluation of Porous Media Permeability Tensors from Pore-Scale Geometry. *Mathematical Geosciences*, 48(3):329–347, April 2016. ISSN 1874-8961, 1874-8953. .

34. Sumit Kumar Singh, Manoj Kumar, Alok Kumar, Abhishek Gautam, and Sunil Chamoli. Thermal and friction characteristics of a circular tube fitted with perforated hollow circular cylinder inserts. *Applied Thermal Engineering*, 130:230–241, February 2018. ISSN 1359-4311. .

35. Sunil Chamoli, Ruixin Lu, Dehao Xu, and Peng Yu. Thermal performance improvement of a solar air heater fitted with winglet vortex generators. *Solar Energy*, 159:966–983, January 2018. ISSN 0038-092X. .

36. Sunil Chamoli, Ruixin Lu, and Peng Yu. Thermal characteristic of a turbulent flow through a circular tube fitted with perforated vortex generator inserts. *Applied Thermal Engineering*, 121:1117–1134, July 2017. ISSN 1359-4311. .

37. Pelin Yazgan-Birgi, Mohamed I. Hassan Ali, and Hassan A. Arafat. Comparative performance assessment of flat sheet and hollow fiber DCMD processes using CFD modeling. *Separation and Purification Technology*, 212:709–722, April 2019. ISSN 1383-5866. .

38. Sunil Chamoli, Ruixin Lu, Jin Xie, and Peng Yu. Numerical study on flow structure and heat transfer in a circular tube integrated with novel anchor shaped inserts. *Applied Thermal Engineering*, 135:304–324, May 2018. ISSN 1359-4311. .

39. Sinthuran Jegatheeswaran, Farhad Ein-Mozaffari, and Jiangning Wu. Process intensification in a chaotic SMX static mixer to achieve an energy-efficient mixing operation of non-newtonian fluids. *Chemical Engineering and Processing - Process Intensification*, 124:1–10, February 2018. ISSN 0255-2701. .

40. Stephen Whitaker. Forced convection heat transfer correlations for flow in pipes, past flat plates, single cylinders, single spheres, and for flow in packed beds and tube bundles. *AIChE Journal*, 18(2):361–371, March 1972. ISSN 0001-1541. .

41. Aurélie Dupuy. Stabilisation de l'interface liquide-liquide dans un contacteur membranaire : Application à l'extraction sélective de terpènes oxygénés d'huile essentielle d'agrumes. April 2010.

42. A. Sengupta, P. A. Peterson, B. D. Miller, J. Schneider, and C. W. Fulk. Large-scale application of membrane contactors for gas transfer from or to ultrapure water. *Separation and Purification Technology*, 14(1):189–200, August 1998. ISSN 1383-5866. .

43. Norfamilabinti Che Mat, Yuecun Lou, and G Glenn Lipscomb. Hollow fiber membrane modules. *Current Opinion in Chemical Engineering*, 4:18–24, May 2014. ISSN 2211-3398. .

44. L. Bao, B. Liu, and G. G. Lipscomb. Entry mass transfer in axial flows through randomly packed fiber bundles. *AIChE Journal*, 45(11):2346–2356, 1999. ISSN 1547-5905. .

45. Steve Elmore and G. Glenn Lipscomb. Analytical approximations of the effect of a fiber size distribution on the performance of hollow fiber membrane separation devices. *Journal of Membrane Science*, 98(1):49–56, January 1995. ISSN 0376-7388. .

46. Ana L. Magalhães, Patrícia F. Lito, Francisco A. Da Silva, and Carlos M. Silva. Simple and accurate correlations for diffusion coefficients of solutes in liquids and supercritical fluids over wide ranges of temperature and density. *The Journal of Supercritical Fluids*, 76:94–114, April 2013. ISSN 0896-8446. .

47. R. Guibert, M. Nazarova, P. Horgue, G. Hamon, P. Creux, and G. Debenest. Computational Permeability Determination from Pore-Scale Imaging: Sample Size, Mesh and Method Sensitivities. *Transport in Porous Media*, 107(3):641–656, April 2015. ISSN 0169-3913, 1573-1634. .

48. Hrvoje Jasak, Aleksandar Jemcov, and Željko Tuković. OpenFOAM: A C++ Library for Complex Physics Simulations. 2007.

49. V. Pozzobon, J. Colin, and P. Perré. Hydrodynamics of a packed bed of non-spherical poly-disperse particles: A fully virtual approach validated by experiments. *Chemical Engineering Journal*, 354:126–136, 2018.

50. Matthias Kind, Holger Martin, Peter Stephan, Wilfried Roetzel, Bernhard Spang, Hans Müller-Steinhagen, Xing Luo, Michael Kleiber, Ralph Joh, and Wolfgang Wagner. VDI Heat Atlas. 2010.